Frascati Physics Series Vol. 73 (2022)
LFC22: Strong interactions from QCD to new strong dynamics at LHC and Future Colliders
August 29 - September 2, 2022

NON-FACTORISABLE CORRECTIONS TO t-CHANNEL SINGLE-TOP PRODUCTION: COMPARING RESULTS FOR THE LHC AND FCC

Christian Brønnum-Hansen
Institute for Theoretical Particle Physics, Karlsruhe Institute of Technology (KIT), Wolfgang-Gaede-Strae 1, 76131 Karlsruhe, Germany
Jérémie Quarroz
Institute for Theoretical Particle Physics, Karlsruhe Institute of Technology (KIT), Wolfgang-Gaede-Strae 1, 76131 Karlsruhe, Germany
Chiara Signorile-Signorile
Institute for Theoretical Particle Physics, Karlsruhe Institute of Technology (KIT), Wolfgang-Gaede-Strae 1, 76131 Karlsruhe, Germany,
Institute for Astroparticle Physics, Karlsruhe Institute of Technology (KIT), Hermann-von-Helmholtz-Platz 1, 76344 Eggenstein-Leopoldshafen, Germany
Chen-Yu Wang
Institute for Theoretical Particle Physics, Karlsruhe Institute of Technology (KIT), Wolfgang-Gaede-Strae 1, 76131 Karlsruhe, Germany
Max-Planck-Institut fr Physik, Fhringer Ring 6, 80805 Mnchen, Germany

Abstract

In this contribution we report on the recent calculation of QCD non-factorisable corrections to t-channel single-top production and stress the importance of these corrections in the light of increasing the accuracy of theoretical predictions for this process. We present results for the total cross section and for selected observables relevant for proton-proton collisions at the LHC and the FCC.

TTP23-006, P3H-23-011

1 Introduction

The large mass and the strong coupling with the Higgs boson makes the top quark a favorite candidate to improve our understanding of the Standard Model, and possibly reveal heavy new physics. A large fraction of the top quarks produced at the LHC emerges from electroweak interactions, via the so-called t-channel single-top production. Predictions for this process can be used, for instance, to constrain the CKM matrix element V_{bt}, and probe possible anomalous couplings in the tWb vertex. QCD corrections to t-channel single-top production are known up to next-to-next-to-leading order (NNLO) in the factorisable approximation [1, 2, 3, 4], namely neglecting the crosstalk between different quark lines (see the left panel of Fig.1 for an example of a Feynman diagram contributing to the factorisable corrections). Factorisable corrections are found to be considerably small and only impact the cross section at $\mathcal{O}(1\%)$. Given the current level of the theory precision, it is useful to go beyond this approximation, and compute the non-factorisable corrections (see the right panel of Fig.1 for an example of Feynman diagram). This contribution vanishes at NLO, due to colour conservation, and it is colour suppressed at NNLO by a factor $N_c^2 - 1 = 8$ with respect to the factorisable corrections. However, it has been recently argued

Table 1: *Comparison of the poles of the two-loop amplitude with the ones predicted using Catani's operator for* $s \sim 104.337\,\mathrm{GeV}^2$ *and* $t \sim -5179.68\,\mathrm{GeV}^2$.

	ϵ^{-2}	ϵ^{-1}
$\langle \mathcal{A}^{(0)} \vert \mathcal{A}^{(2)}_{\mathrm{nf}} \rangle$	$-229.0940408654660 - 8.978163333241640i$	$-301.1802988944764 - 264.1773596529505i$
Catani	$-229.0940408654665 - 8.978163333241973i$	$-301.1802988944791 - 264.1773596529535i$

that an enhancement factor π^2, due to the Glauber phase, may enhance non-factorisable corrections and compensate for the colour suppression. This effect was explicitly proven to occur in the calculation of non-factorisable corrections to the vector boson fusion in the eikonal approximation [5].

In this document we summarise the results obtained for the non-factorisable corrections to t-channel single-top production [6, 7, 8] and discuss their relevance for 13 TeV and 100 TeV proton-proton collisions.

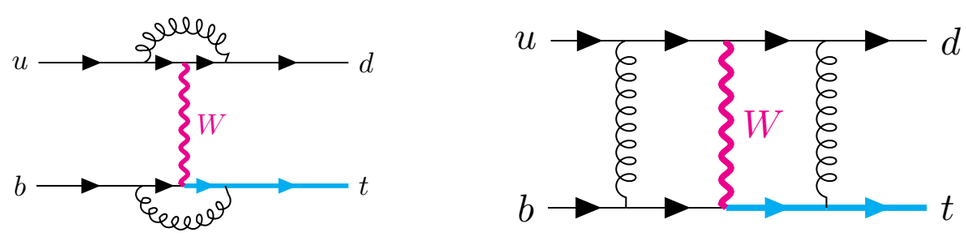

Figure 1: *Left panel: example of Feynman diagram contributing to factorisable corrections. Right panel: example of diagram contributing to non-factorisable corrections. Massless quarks are indicated with thin black line, while the massive top-quark is depicted with a blue solid line.*

2 Ingredients of the calculation

One crucial ingredient for the calculation is the double-virtual correction. In this regard, the most challenging part is the evaluation of the two-loop amplitude associated to non-factorisable diagrams as in the right panel of Fig. 1. The double-virtual amplitude is obtained numerically through the auxiliary mass flow method [10, 11]. We refer the reader to Ref. [6] for further details. Here we emphasise that the reduction of the amplitude is done analytically, retaining the full dependence on the kinematic scales s, t, m_W and m_t. The evaluation of the master integrals can be performed to any desired accuracy within a modest computing time (for a typical phase space point, 20 digits accuracy can be reached in about 30 minutes on a single core). In Tab. 2, we present the poles obtained for the two-loop amplitude compared to those predicted by Catani's operator [9]. The match between the two values degrades by only one digit per ϵ-order, starting with an agreement of 15 digits at ϵ^{-2}. We then expect a 13 digits accuracy for the finite part. To evaluate the cross section, we prepare a grid optimised for the Born cross section. We extract 10 independent sets of 10^4 points from this grid and evaluate the amplitude for each of these points. The resulting accuracy can be estimated to be $\mathcal{O}(2\%)$.

A further non-trivial element of the calculation is the evaluation of real-virtual amplitudes, and of the corresponding cross-section level contribution. The challenge is related to the presence of numerous mass scales and to the necessity of having stable results also in kinematic regions where the extra radiation becomes unresolved. We note that working with unticommuting γ_5 in d dimensions, we can calculate

form factors treating the weak current as a pure vector current, while fixing the external massless quarks to be left-handed. To treat the form factors we manage to express the real-virtual amplitude in terms of scalar box, triangle and bubble integrals. To improve the numerical stability of the amplitude, we switch to a basis of finite box integrals, restricting the divergent part to triangle integrals only, whose coefficients either become independent of the dimensional regulator ϵ or simply vanish.

The last contribution is the tree-level, double-real correction, which involves the emission of two, potentially unresolved, gluons that connect the massive and the massless quark lines. Real emission contributions are known to develop soft and collinear (IR) singularities and therefore cannot be evaluated directly (see for instance Ref. [12] for a recent review on the topic). In our analysis we exploit the nested soft-collinear subtraction scheme [13] to handle this issue and obtain fully differential results. For the process at hand, only soft singularities can affect real-radiation amplitudes, and they are only related to independent emissions, namely to Abelian-like interactions. This observation simplifies remarkably the subtraction procedure, which indeed requires a limited number of counterterms. When integrating over the energies and emission angles of unresolved partons, the IR singularities encoded in the counterterms turn into poles in ϵ, which cancel against those stemming from virtual and real-virtual corrections. A small complication arises from having massive emitters. However, phase space integration can be performed analytically and returns compact results.

3 Phenomenology at the LHC and at the FCC

We consider proton-proton collisions at 13 TeV and at 100 TeV. We use the `CT14` set for parton distribution functions (PDF) and the strong coupling constant. We match the perturbative order of the cross section to that of the PDF set, and use the following input parameters: $v = 246.2$ GeV, $m_W = 80.379$ GeV, and $m_t = 173.0$ GeV.
We first present the integrated cross section at a fixed factorisation scale $\mu_F = m_t$ at 13 TeV

$$\frac{\sigma_{pp\to X+t}}{1\,\text{pb}} = 117.96 + 0.26 \left(\frac{\alpha_s(\mu_R)}{0.108}\right)^2 . \tag{1}$$

We stress that non-factorisable corrections arise for the first time at NNLO, and therefore there is not a clear indication of an optimal choice of renormalisation scale. From Eq.1, it is clear that changing the value of μ_R can substantially modify the impact of these corrections. For instance, considering the renormalisation scale $\mu_R = m_t$, the non-factorisable corrections amount to about 0.2% of the LO cross section. If instead we set μ_R to the typical transverse momentum of the top quark, $\mu_R = 40\,\text{GeV}$, non-factorisable corrections reach 0.35% of the LO cross section. Although tiny, non-factorisable corrections are quite comparable to the NNLO factorisable corrections to the NLO cross section. The latter were computed to be about -0.7% for similar choices of scales and parton distribution functions (see Table 7 in Ref. [4]).[1] To further analyse the effects of different scale choices, in Tab. 3 we report the LO cross section and the corresponding non-factorisable corrections for different values of the minimal top-quark transverse momentum ($p_\perp^{t,cut}$). We fixed $\mu_F = m_t$ and vary the renormalisation scale. For $\mu_R = m_t$ we also include scale variations corresponding to $\mu_R/2$ and $2\mu_R$. We notice that, while the LO cross section decreases by $\mathcal{O}(11\%)$ if the $p_\perp^t$ cut increases from 0 to 60 GeV, the non-factorisable contribution to the cross section increases by $\mathcal{O}(8\%)$, both for $\mu_R = m_t$ and $\mu_R = 40$ GeV.

[1] Computations in Ref. [4] were performed for proton-proton collisions at 14 TeV.

Table 2: *Dependence of the LO cross section and the non-factorisable corrections on the transverse momentum of the top quark for different values of the renormalisation scale, at $\mu_F = m_t$. For each scale choice, we report the relative impact, $\delta_{\rm NNLO}$, of the non-factorisable contributions with respect to the LO cross section. See Ref.* [7] *and the text for further details.*

		$\mu_R = m_t$		$\mu_R = 40$ GeV	
$p_\perp^{t,cut}$	$\sigma_{\rm LO}$ (pb)	$\sigma^{\rm nf}_{\rm NNLO}$ (pb)	$\delta_{\rm NNLO}$ [%]	$\sigma^{\rm nf}_{\rm NNLO}$ (pb)	$\delta_{\rm NNLO}$ [%]
0 GeV	118.01	$0.26^{-0.04}_{+0.06}$	$0.22^{-0.04}_{+0.05}$	0.40	0.34
20 GeV	115.09	$0.26^{-0.04}_{+0.06}$	$0.23^{-0.04}_{+0.05}$	0.41	0.36
40 GeV	109.56	$0.27^{-0.05}_{+0.06}$	$0.25^{-0.04}_{+0.06}$	0.43	0.39
60 GeV	104.63	$0.28^{-0.05}_{+0.06}$	$0.26^{-0.04}_{+0.06}$	0.43	0.41

Table 3: *Dependence of the LO cross section and the non-factorisable corrections on the transverse momentum of the top quark for different values of the renormalisation scale, at $\mu_F = m_t$ and $\sqrt{S}$= 100 TeV. Similarly to Tab. 3, for each scale choice we report the relative impact, $\delta_{\rm NNLO}$, of the non-factorisable contributions with respect to the LO cross section. See Ref.* [8] *and the text for further details.*

		$\mu_R = m_t$		$\mu_R = 40$ GeV	
$p_\perp^{t,cut}$	$\sigma_{\rm LO}$ (pb)	$\sigma^{\rm nf}_{\rm NNLO}$ (pb)	$\delta_{\rm NNLO}$ [%]	$\sigma^{\rm nf}_{\rm NNLO}$ (pb)	$\delta_{\rm NNLO}$ [%]
0 GeV	2367.02	$3.79^{-0.63}_{+0.84}$	$0.16^{-0.03}_{+0.04}$	5.95	0.25
20 GeV	2317.03	$3.89^{-0.64}_{+0.86}$	$0.17^{-0.03}_{+0.04}$	6.11	0.26
40 GeV	2216.61	$4.14^{-0.69}_{+0.92}$	$0.19^{-0.03}_{+0.04}$	6.50	0.29
60 GeV	2121.88	$4.28^{-0.71}_{+0.95}$	$0.20^{-0.03}_{+0.04}$	6.71	0.32

We now present the results for the integrated cross-section at 100 TeV

$$\frac{\sigma_{pp\to X+t}}{1\,\text{pb}} = 2367.0 + 3.8\left(\frac{\alpha_s(\mu_R)}{0.108}\right)^2 . \tag{2}$$

For a renormalisation scale $\mu_R = m_t$, the NNLO corrections amount to 0.16%, and increase to 0.25% for $\mu_R = 40\,\text{GeV}$. In order to compare the two energy regimes, 13 and 100 TeV, we repeat the analysis presented in the previous paragraph and report in Tab. 3 the impact of imposing different cuts on the top-quark transverse momentum and varying the renormalisation scale. We notice that, for a center-of-mass energy of 100 TeV, the LO cross-section manifests a relative decrease of $\mathcal{O}(10\%)$ when setting $p_\perp^{t,cut} = 60$ GeV. This behaviour is comparable with the one observed at 13 TeV. On the other hand, non-factorisable corrections increase by a slightly larger amount with respect to the 13 TeV result: $\mathcal{O}(13\%)$ for both $\mu_R = m_t$ and $\mu_R = 40$ GeV.

We then consider differential distributions, and study the the impact of the non-factorisable corrections on the top-quark transverse momentum. In Fig. 2 we plot with a blue solid line the LO contribution, with a red dashed line the non-factorisable corrections at $\mu \equiv \mu_F = \mu_R = m_t$ (the corresponding scale variation is denoted by the striped region), and with a green dashed line the non-factorisable corrections at $\mu = 40$ GeV. We notice from Fig. 2 that for both $\sqrt{S} = 13$ TeV and $\sqrt{S} = 100$ TeV, the non-factorisable corrections are $p_\perp^t$-dependent and manifest a similar shape. For instance, they are relatively small and negative at low values of the transverse momentum. This behaviour is compatible with the one of the

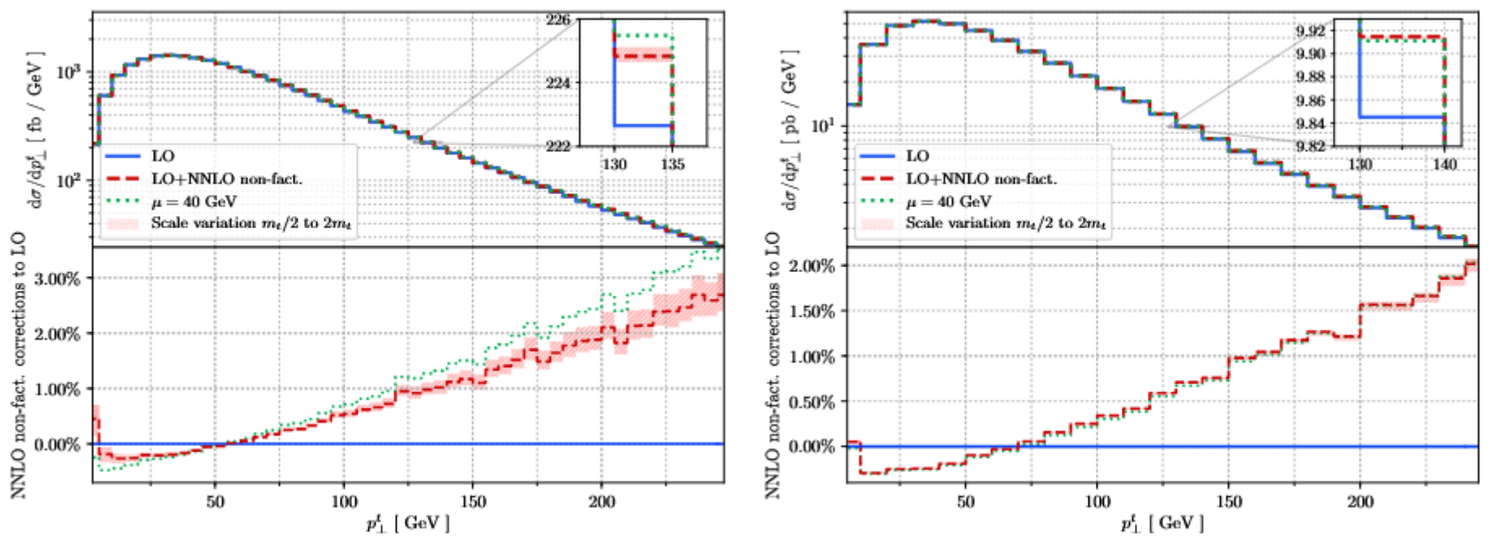

Figure 2: *Top quark transverse momentum distribution for $\sqrt{S} = 13$ TeV (left panel) and $\sqrt{S} = 100$ TeV (right panel). The blue solid line represents the Born cross section. The red dashed line corresponds to the non-factorisable corrections at $\mu \equiv \mu_F = \mu_R = m_t$. The striped region denotes the scale variation band. We also present with a green dotted line the $p_\perp^t$ distribution at $\mu = 40$ GeV.*

double-virtual correction, presented in Ref. [6], which we expect to be kinematically favoured at low $p_\perp^t$. In contrast, we observe that the sign of the corrections changes at different values of $p_\perp^t$ depending on $\sqrt{S}$: around 70 GeV for $\sqrt{S} = 100$ TeV and around 50 GeV for $\sqrt{S} = 13$ TeV.

We turn to the analysis of jet observables and focus on the transverse momentum distribution of the leading jet. To define jets we use the $k_\perp$-algorithm [14] and require them to have transverse momenta larger than 30 GeV and a radius of $R = 0.4$. From Fig. 3 we observe that the corrections to the leading-jet

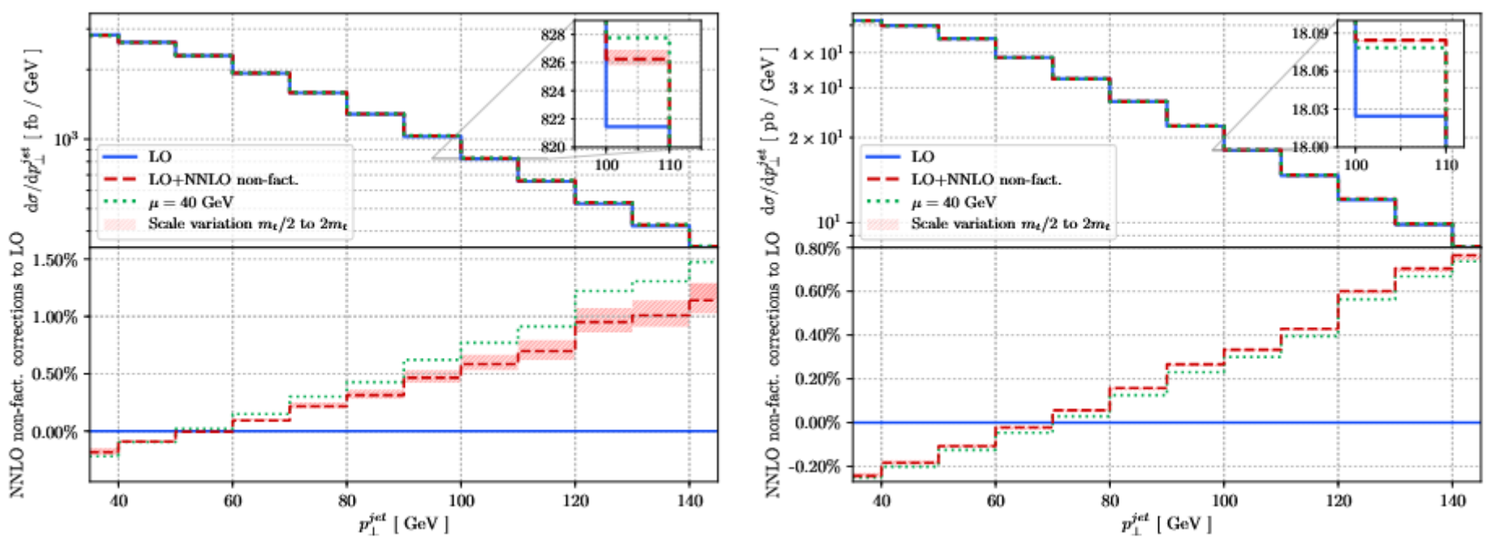

Figure 3: *Leading jet transverse momentum distribution for $\sqrt{S} = 13$ TeV (left panel) and $\sqrt{S} = 100$ TeV (right panel).See the caption of Fig. 2 for details about the colors code.*

transverse momentum are negative for $p_\perp^{jet}$ smaller than ~ 50 GeV and reach about 1% at $p_\perp^{jet} \sim 140$ GeV for $\sqrt{S} = 13$ TeV. In contrast, at $\sqrt{S}$ =100 TeV the corrections change sign around 70 GeV and reach 0.7% at $p_\perp^{jet} \sim 140$ GeV.

4 Conclusions

In this manuscript, we have reported on the recent calculation of *non-factorisable* corrections to the t-channel single-top production. This contribution was previously neglected by invoking its color suppression with respect to factorisable corrections, known since many years. The present calculation completes the estimate of NNLO corrections to the t-channel single-top production, and proves that the methods used to overcome the technical challenges are sufficiently robust to produce phenomenologically relevant results. We have investigated the impact of non-factorisable corrections on the inclusive cross section and on a number of kinematic distributions, for proton-proton collisions at 13 and 100 TeV. For collisions at 13 TeV, we have shown that non-factorisable contributions can become quite comparable to the factorisable ones in selected regions of the phase space. At 100 TeV, a direct comparison is not yet available due to the lack of results for the factorisable component. Such comparison would be beneficial for a deeper understanding of the relative importance of the two classes of corrections, encouraging similar analysis for different processes.

5 Acknowledgements

The authors thank Prof. Kirill Melnikov for contributing to the results quoted in this report. This research is partially supported by the Deutsche Forschungsgemeinschaft (DFG, German Research Foundation) under grant 396021762 - TTR 257. CBH acknowledges support from the Carlsberg Foundation.

References

1. M. Brucherseifer *et al*, Phys. Lett. B **736**, 58 (2014).
2. E. L. Berger *et al*, Phys. Rev. D **94**, 7 (2016).
3. E. L. Berger *et al*, JHEP **11**, 158 (2017).
4. J. Campbell *et al*, JHEP **02**, 040 (2021).
5. T. Liu *et al*, Phys. Rev. Lett. **123**, 12 (2019).
6. C. Brønnum-Hansen *et al*, JHEP **11**, 130 (2021).
7. C. Brønnum-Hansen *et al*, JHEP **06**, 061 (2022).
8. C. Brønnum-Hansen *et al*, PoS LL2022, 035 (2022).
9. S. Catani, Phys. Lett. B **427**, 161 (1998).
10. X. Liu *et al*, Phys. Lett. B **779**, 353 (2018).
11. X. Liu *et al*, Chin. Phys. C **45**, 1 (2021)
12. N. Agarwal *et al*, Phys. Rept. **994**, 1 (2023).
13. F. Caola *et al*, Eur. Phys. J. C **77**, 248 (2017)
14. S. D. Ellis *et al*, Phys. Rev. D **48**, 3160 (1993)

Frascati Physics Series Vol. 73 (2022)
LFC22: Strong interactions from QCD to new strong dynamics at LHC and Future Colliders
August 29 - September 2, 2022

Top pair entanglement in the SMEFT

Rafael Aoude
Centre for Cosmology, Particle Physics and Phenomenology (CP3),
Université Catholique de Louvain, 1348 Louvain-la-Neuve, Belgium

Abstract

Entanglement is a very powerful tool to explore properties of quantum states and their evolution. In this work, the spin entanglement in top pair production is explored within the framework of the Standard Model Effective Field Theory (SMEFT). In particular, we explore two regions of the phase space where the Standard Model produces maximally entangled states: the high-energy limit and at production threshold. We study the pattern in the $q\bar{q}$, gg and the pp initiated channels. In general, we have observed that higher-dimensional operators lower the entanglement produced purely by the Standard Model.

1 Introduction

In a recent work [1], the authors have explored the spin-entanglement of a top pair produced by Standard Model (SM) interactions at the Large Hadron Collider (LHC). Top quarks have two main advantages compared to other particles: they decay faster than their hadronization scale and therefore their spin information is directly transmitted to the decay products and they can be characterized by a simple bipartite qubit system. Since this work, many other studies have appear on top spin-entanglement [10, 11, 12, 13] but also on other SM process such as photon pairs, $\tau\tau$, and diboson [12, 14, 15, 16, 17, 18]

The authors also proposed an experimental strategy to detect entanglement based on measuring the differential cross-section with respect to the decay products' angle, in particular the angular separation of the charged leptons of each top. Furthermore, they have shown that there are two regions in the phase-space of *maximal entanglement*: for very high-energies $\hat{s} \to \infty$ and $\theta = \pi/2$ and at threshold $\hat{s} = 2m_t$. In these regions, the quantum state of the top pair is a triplet and singlet, respectively.

In this study [2], with the final goal of studying the underlying theory of the SM, we use the SMEFT framework to explore two main questions:

- Are the Standard Model maximally-entangled regions affected by the SMEFT?
- Can the SMEFT induce new different maximally-entangled regions in the phase-space?

2 Top pair spin correlations

The study of the entanglement in spin-space is given in terms of the spin correlation matrix, also called the R-matrix

$$R^I_{\eta_1\eta_2,\zeta_1\zeta_2} = \frac{1}{N_a N_b} \sum_{\substack{\text{colors}\\ \text{spins}}} \mathcal{M}^*_{\eta_2\zeta_2}\mathcal{M}_{\eta_1\zeta_2} \qquad \text{with} \qquad \mathcal{M}_{\eta\zeta} \equiv \langle t(k_1,\eta)\bar{t}(k_2,\zeta)|\mathcal{T}|a(p_1)b(p_2)\rangle \tag{1}$$

where $\mathcal{T}$ is the transition matrix and $I = ab$ denotes the possible initial state, i.e $I = q\bar{q}, gg$ at leading-order and $N_{a,b}$ represents the number of degrees of freedom in the initial states a and b. This matrix can be rewritten using the Fano decomposition [3)]

$$R = \tilde{A}\,\mathbb{1}_2 \otimes \mathbb{1}_2 + \tilde{B}^+_i \sigma^i \otimes \mathbb{1}_2 + \tilde{B}^-_i \mathbb{1}_2 \otimes \sigma^i + \tilde{C}_{ij}\sigma^i \otimes \sigma^j, \tag{2}$$

where the summations over repeated indices are implicit and the first coefficient $\tilde{A}$ is related to the cross-section. This matrix has to be properly normalized by taking $\rho = R/\mathrm{tr}(R)$, which can be decomposed using the same Fano decomposition, in terms of Pauli matrices. The normalized coefficients are given by $B^\pm_i = \tilde{B}^\pm_i/\tilde{A}$ and $C_{ij} = \tilde{C}_{ij}/\tilde{A}$.

The R^I matrix for a given state is not representative of the initial state at the LHC in proton-proton collisions, where at leading-order, the gg- and $q\bar{q}$-initiated channels contribute non-interfering. Hence, the initial quantum state is mixed and it is given by the weighted sum of both channels: $R(\hat{s}, \boldsymbol{k}) = \sum_I L^I(\hat{s}) R^I(\hat{s}, \boldsymbol{k})$, where $L^I(\hat{s})$ are the luminosity functions for each channel given in [4)].

Once each matrix is obtained, we further calculate these coefficients in the so-called *helicity basis*, which consists of a centre-of-mass orthonormal frame:

$$\{\boldsymbol{k}, \boldsymbol{n}, \boldsymbol{r}\}: \qquad \boldsymbol{r} = \frac{\boldsymbol{p} - z\boldsymbol{k}}{\sqrt{1-z^2}}, \qquad \boldsymbol{n} = \boldsymbol{k} \times \boldsymbol{r} \tag{3}$$

where $\boldsymbol{p}$ and $\boldsymbol{k}$ are unit vectors along the beam axis and the top direction with $z \equiv \boldsymbol{k}\cdot\boldsymbol{p}$. In this basis, the entanglement measure becomes very simple, as we are going to see in the following. But before, note that the spin density matrix, at LO in QCD, simplifies due to: invariance under CP, which implies symmetric C_{ij} and $B^+_i = B^-_i$; non-zero C_{kn}, C_{rn} and $B^\pm_n$ are only non-vanishing at one-loop; and, finally, $B^\pm_k = B^\pm_r = 0$, since interactions are P-even. For SMEFT, the two first statements still holds since we focus on CP even operators.

3 Entanglement in the SM(EFT)

For the most general bipartite quantum state acting on the Hilbert space $\mathcal{H}_{\mathrm{ab}} = \mathcal{H}_{\mathrm{a}} \otimes \mathcal{H}_{\mathrm{b}}$, if the state can be written as a convex combination of product states $p_{\mathrm{ab}} = \sum_k p_k \rho^k_{\mathrm{a}} \otimes \rho^k_{\mathrm{b}}$, the state is separable. If the state cannot be taken to this form, we say the state is entangled. However, it is more practical to use entanglement measures to quantify it. We have used the concurrence [5)] and the Peres-Horodecki Criterion (PHC) [6, 7)]. For the LO-QCD density matrix in the helicity basis, the PHC implies

$$\Delta[\rho] \equiv -C_{nn} + |C_{kk} + C_{rr}| - 1 > 0 \tag{4}$$

as a sufficient condition for entanglement. For the SM, at LO-QCD, the condition $\Delta > 0$ is a necessary condition and the concurrence can be written in a simple form as $C[\rho] = \max(\Delta/2, 0)$. For higher orders in SMEFT, the explicit analytical results can be found in App. C of [2)].

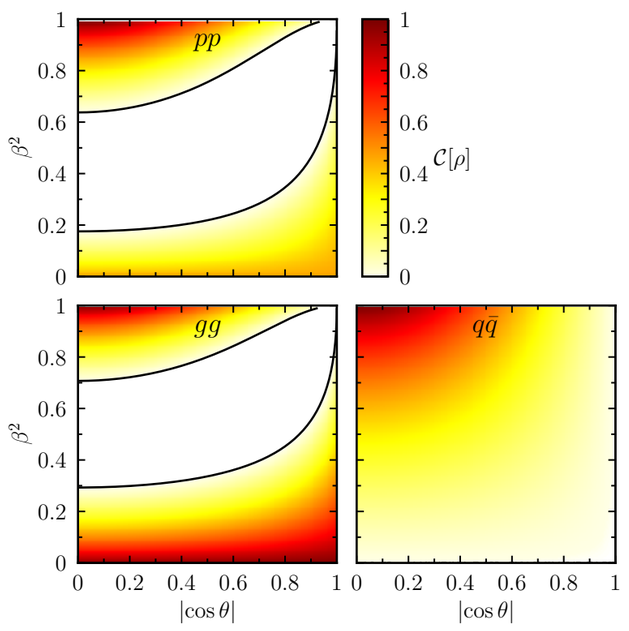

Figure 1: SM contribution for the concurrence in the $q\bar{q}$- (bottom right) and gg-initiated (bottom left) channels, as well as in the full pp collision (top).

We first start with the SM, in particular the LO-QCD. For this case, we have reproduced the results from [1], which gives the plots in Fig. 1. For the gg-channel, we have two regions of maximal entanglement, at threshold $\beta = 0$, regardless of $z = \cos\theta$, and at high-energy ($\beta = 1$) and $\cos\theta = 0$. These produced quantum states are Bell states, where the former is given by a singlet and the latter by a triplet:

$$\rho_{gg}^{\rm SM}(0,z) = |\Psi^-\rangle_{\boldsymbol{n}}\langle\Psi^-|_{\boldsymbol{n}}, \quad \rho_{gg}^{\rm SM}(1,0) = |\Psi^+\rangle_{\boldsymbol{n}}\langle\Psi^+|_{\boldsymbol{n}}, \tag{5}$$

while for the $q\bar{q}$-channel we only have one maximally entangled state at high energies

$$\rho_{q\bar{q}}^{\rm SM}(1,0) = |\Psi^+\rangle_{\boldsymbol{n}}\langle\Psi^+|_{\boldsymbol{n}}, \tag{6}$$

and it is entangled across all the phase-space expected at threshold, which is separable. Given these conclusions for the SM, we would like to answer the questions raised in the introduction for Fig. 1 and the maximally entangled quantum states. The SMEFT Lagrangian is formulated as

$$\mathcal{L}_{\rm SMEFT} = \mathcal{L}_{\rm SM} + \frac{1}{\Lambda^2}\sum_i c_i \mathcal{O}_i + \cdots \tag{7}$$

where we work only with CP-even operators at dimension six. The relevant operators for our analysis are [8]

$$\mathcal{O}_G = g_s f^{ABC} G_\nu^{A,\mu} G_\rho^{B,\nu} G_\mu^{C,\rho}\,, \quad \mathcal{O}_{\varphi G} = \left(\varphi^\dagger\varphi - \frac{v^2}{2}\right) G_A^{\mu\nu} G_{\mu\nu}^A\,, \quad \mathcal{O}_{tG} = g_s(\bar{Q}\sigma^{\mu\nu}T^A\, t)\tilde{\varphi} G_{\mu\nu}^A + \text{h.c.}\,, \tag{8}$$

where φ is the Higgs doublet, as well as the color-octet and -singlet four-fermion operators

$$\mathcal{O}_{Qq}^{(8,1)} = (\bar{Q}_L\gamma_\mu T^a Q_L)(\bar{q}_L\gamma^\mu T^a q_L)\,, \qquad \mathcal{O}_{Qq}^{(8,3)} = (\bar{Q}_L\gamma_\mu T^a\sigma^A Q_L)(\bar{q}_L\gamma^\mu T^a\sigma^A q_L)\,, \tag{9}$$

$$\mathcal{O}_{tu}^{(8)} = (\bar{t}_R\gamma_\mu T^a t_R)(\bar{u}_R\gamma^\mu T^a u_R)\,, \qquad \mathcal{O}_{td}^{(8)} = (\bar{t}_R\gamma_\mu T^a t_R)(\bar{d}_R\gamma^\mu T^a d_R)\,, \tag{10}$$

$$\mathcal{O}_{Qu}^{(8)} = (\bar{Q}_L\gamma_\mu T^a Q_L)(\bar{u}_R\gamma^\mu T^a u_R)\,, \qquad \mathcal{O}_{Qd}^{(8)} = (\bar{Q}_L\gamma_\mu T^a Q_L)(\bar{d}_R\gamma^\mu T^a d_R)\,, \tag{11}$$

$$\mathcal{O}_{tq}^{(8)} = (\bar{t}_R\gamma_\mu T^a t_R)(\bar{q}_L\gamma^\mu T^a q_L)\,, \tag{12}$$

with the corresponding singlet operators given by the same expressions but without the $SU(3)$ generators T^a. Here, Q_L and q_L denote heavy and light left-handed quark doublets, respectively, and u_R and d_R are the right-handed light quarks.

To understand its effect, we come back to the R-matrix, expanding the SM and the EFT part and normalizing it as

$$\rho = \frac{R^{\rm SM} + R^{\rm EFT}}{\text{tr}(R^{\rm SM}) + \text{tr}(R^{\rm EFT})} \tag{13}$$

As stated before, the new density matrix can be written in terms of the Fano decomposition and all the explicit SMEFT contribution to these terms can be found in the Appendix A of the original paper [2].

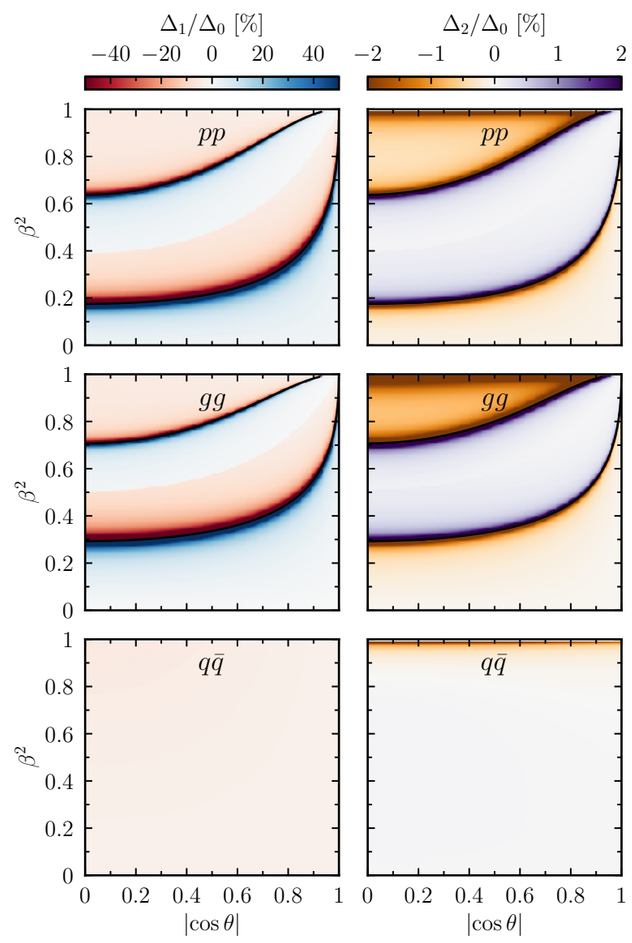

Figure 2: Relative contributions of the linear (left) and quadratic (right) effects of the chromomagnetic operator for $c_{tG}/\Lambda^2 = 0.1$ TeV^{-2} to the PHC entanglement marker Δ.

Since the R-matrix includes a product of two scattering amplitudes expanded in Λ^{-2}, we will consider two types of terms: linear $\mathcal{O}(\Lambda^{-2})$ and quadratic $\mathcal{O}(\Lambda^{-4})$. To examine these contributions, we will consider the entanglement marker Δ at the desired order compared to the SM marker Δ_0. Hence, for the linear order we define $\Delta_1 \equiv \Delta - \Delta_0$ where Δ is calculated with the ρ up to linear order. Similarly, we define $\Delta_2 \equiv \Delta - (\Delta_0 + \Delta_1)$ where ρ now also includes the squared contributions.

In Figure 2, we show an example plot for these markers. In particular, we show Δ_1/Δ_0 and Δ_2/Δ_0 for the operator $\mathcal{O}_{tG}$ with the value of the Wilson coefficient given by $c_{tG} = 0.1\text{TeV}^{-2}$. In general, for the gg-channel, three operators contribute $\mathcal{O}_{tG}$, $\mathcal{O}_G$ and $\mathcal{O}_{\varphi G}$. At threshold, all the linear interference effects vanish and the SMEFT does not affect the maximally entangled points induced by the SM, which is not generally true across the phase-space. At quadratic order, the story is different and although the operator $\mathcal{O}_{\varphi G}$ has a vanishing contribution, $\mathcal{O}_G$ and $\mathcal{O}_{tG}$ induce an entanglement decrease across the phase space and especially at the SM maximal points. For the latter, this can be seen in Figure 2 by the orange regions. In the $q\bar{q}$ initiated channel we have a similar pattern in the sense that there are no contributions to the marker Δ at threshold (both linear and quadratic) whereas at high energies, both effects may modify the level of entanglement around the SM point of maximal entanglement. In this region, the quadratic contribution of the latter always decreases the concurrence at high p_T and the linear one depends on the sign of the respective Wilson coefficient. The threshold quantum states are then modified to

$$\rho_{gg}^{\text{EFT}}(0,z) = p_{gg}|\Psi^+\rangle_{\text{p}}\langle\Psi^+|_{\boldsymbol{p}} + (1-p_{gg})|\Psi^-\rangle_{\boldsymbol{p}}\langle\Psi^-|_{\boldsymbol{p}}, \tag{14}$$

$$\rho_{q\bar{q}}^{\text{EFT}}(0,z) = p_{q\bar{q}}|\uparrow\uparrow\rangle_{\boldsymbol{p}}\langle\uparrow\uparrow|_{\boldsymbol{p}} + (1-p_{q\bar{q}})|\downarrow\downarrow\rangle_{\boldsymbol{p}}\langle\downarrow\downarrow|_{\boldsymbol{p}} \tag{15}$$

where $p_{gg} = 72m_t^2(3\sqrt{2}m_t c_G + v c_{tG})^2/7\Lambda^4$ and $p_{q\bar{q}} = \frac{1}{2} - 4c_{VA}^{(8),u}/\Lambda^2 + \mathcal{O}(1/\Lambda^4)$. For the gg-initiated, SMEFT induces a triple state at quadratic order while for $q\bar{q}$ the eigenvalues of the matrix are affected. For the high-p_T region, the analysis is more subtle since we cannot reach $\beta \to 1$, where the EFT validity breaks down. However, for high enough energies and below the cut-off scale, the quadratic contribution again decreases the entanglement while the linear one depends on the Wilson coefficient sign.

4 Conclusion

In this work, we have explored the possibility of quantum observables, such as entanglement, to assess the impact of new physics effects in high-energy interactions. Two main entanglement measures were used, PHC and concurrence, to explore how the linear and quadratic SMEFT effects change the SM maximal entanglement. Overall, we have observed that linear higher-dimensional effects tend to vanish